

Direct observation of the vanishing EELS cross section in graphene

Alberto Guandalini,¹ Ryosuke Senga,² Yung-Chang Lin,² Kazu Suenaga,^{2,3} Paolo Barone,^{4,1} Francesco Mauri,¹ Thomas Pichler,⁵ and Christian Kramberger^{3,5}

¹*Dipartimento di Fisica, Università di Roma La Sapienza, Piazzale Aldo Moro 5, I-00185 Roma, Italy**

²*AIST Tsukuba, 1-1-1 Umezono, Tsukuba, Ibaraki 305-8560 Japan*

³*The Institute of Scientific and Industrial Research (SANKEN),
Osaka University Mihogaoka 8-1, Ibaraki, Osaka 567-0047, Japan*

⁴*CNR-SPIN, Area della Ricerca di Tor Vergata,
Via del Fosso del Cavaliere 100, I-00133 Rome, Italy*

⁵*University of Vienna, Faculty of Physics, Strudlhofgasse 4, A1090, Austria*

In transmission electron energy-loss spectroscopy, the cross section in 2D is quenched by kinematic effects once the momentum transfer becomes smaller than a critical value set by q_z , the momentum loss parallel to the beam. Our highly momentum ($\Delta q = 0.02 \text{ \AA}^{-1}$) and energy ($\Delta E = 45 \text{ meV}$) resolved setup is instrumental on delivering the unprecedented experimental verification of quenched 2D EEL spectra on freestanding graphene at momentum transfers q below 0.06 \AA^{-1} . We retrieve the intrinsic uniform dielectric response of graphene from measured spectra by quantifying the kinematic suppression.

Electron energy-loss spectroscopy (EELS) is a powerful tool to investigate electronic excitations in materials, as it directly probes the longitudinal dielectric response of the system, in principle resolved both in energy and momentum [1, 2]. Special attention is often devoted to vanishing momentum transfer, also referred to as the optical limit, where the cross section contains the same information delivered by the optical response of the sample [3, 4]. Energy resolution of few meV can be attained, e.g., by using low-energy electrons that are reflected by the sample surface, the scattering angle enabling the measure of the momentum transfer and thus providing access to the excitation's dispersion with a momentum resolution that has been recently pushed down to 10^{-3} \AA^{-1} [5]. This technique, known as high-resolution EELS (HREELS), is however a surface-sensitive one, and as such it cannot probe the bulk response of the target material, since the scattered electrons hardly penetrate it. On the contrary, higher energy electrons as those used in a transmission electron microscope (TEM) can pass through a target of about $1 \mu\text{m}$ thickness [6]. A sketch of the experimental geometry is shown in the left panel of Fig. 1. If the thickness d of the sample is such that $q_{3D}d \gg 1$, where $q_{3D} = |\mathbf{k}_i - \mathbf{k}_f|$ is the momentum lost by the beam electron, the loss function can be modelled within inelastic scattering theory by approximating the dielectric response of the film with that of the bulk [6–8]. Otherwise, finite thickness effects become relevant. Recent years have witnessed a significant effort in optimizing both energy and momentum resolution of TEM-EELS, reaching few tens of meV and few hundredths of \AA^{-1} , respectively [9–15]. Such advancement of the experimental setup has made TEM-EELS a valuable tool for studying bulk fundamental excitations as a function of momentum transfer in small volumes of material [16–20].

The angular and energy dependence of the inelastic electron scattering are specified by a double-differential cross section, that can be generally expressed as the product of two terms: the so-called loss function, accounting for the target response to an incident electron, and a kinematic prefactor that instead only depends on the scattering geometry through energy and momentum conservation [1, 2]. The kinematic prefactor, crucial in the interpretation of HREELS spectra [21–25] because of the dependence of the momentum transfer on both the scattering angle and the energy loss [1], is generally simplified in TEM-EELS, where the momentum transfer is regarded to lie only within the plane perpendicular to the incoming electron beam [26]. This assumption is reasonable in typical experimental setups with small scattering angles and momentum resolution of few tenths of \AA^{-1} limiting the access to the low-momentum transfer regime, and as long as the targeted film is thick enough to be viewed as a bulk 3D sample. The TEM-EELS cross section is thus proportional to $-\text{Im}[\varepsilon^{-1}(q_{3D}, \omega)]/q_{3D}^2$, with the energy loss $\hbar\omega$, where the loss function is given by the bulk 3D inverse dielectric function ε^{-1} .

In the last decades, particular attention has been devoted to the study of 2D materials, i.e., materials that are periodic in two directions (x, y) and atomically thin in the third direction (z), due to their remarkable electronic and optical properties [27, 28]. Their intrinsic dielectric response, that in HREELS measurements is affected by the inevitable presence of substrates, can be naturally accessed by TEM-EELS enabling the study of electronic [14, 29] and lattice [9, 13] excitations of freestanding 2D materials. When the sample thickness becomes atomic and/or the system is probed near to the optical limit, dimensionality effects may arise in the dielectric response due to the partially confined nature of the electrons. In this regime, the system response becomes anisotropic, and one conveniently decomposes the momentum lost by the incoming electrons \mathbf{q}_{3D} in \mathbf{q} and q_z , the momentum transfer parallel and perpendicular, respectively, to the xy plane of the system (see left panel of Fig. 1). While \mathbf{q} is transferred to the

crystal quasi-momentum of the 2D periodic lattice, thus being a good quantum number for the material's electrons, q_z is not. The latter encodes the dependence of the momentum transfer on the energy loss, while the intrinsic response of the system depends mainly on \mathbf{q} [1, 26]. We point out that these considerations, relevant for 2D materials, apply also to thin films, as the interpretation of EEL spectra in terms of the 3D response is an approximation valid only for $q_{3D}d \gg 1$.

Transmission EELS has been studied at different levels of theory mostly within a 3D framework [1, 8, 30]. Nonetheless, the relation between the measured EELS cross section and the dielectric response of a 2D system has been recently addressed by Nazarov [31], showing that it indeed differs from the 3D response. As an example, the kinematic term for the case of a 2D system at low momentum transfers significantly differs from the bulk counterpart, due to the $\approx e^{-qz}$ decay of electric fields in the vacuum. In this regime, the 2D material may be approximated as a 2D sheet [32], displaying qualitatively different dielectric properties [33]. Remarkably, it has been theoretically predicted that the cross section of a 2D material vanishes in the low-momentum transfer regime instead of giving a maximum signal as the $1/q_{3D}^2$ prefactor would predict, due to the inability of 2D materials to screen the Coulomb interaction in the long-wavelength limit [31]. A TEM setup allowing for a very high momentum resolution is instrumental to probe the 2D features of the kinematic response, that we anticipate occur at $q \leq q_z$.

In this work, we study the EEL cross section of a prototypical 2D material, graphene, in the optical limit regime, i.e. at low-momentum transfers ($q < 0.1 \text{ \AA}^{-1}$). Graphene is one of the most studied 2D materials due to its potential electronic applications, e.g., for plasmonic and electronic devices [34–37]. The energy loss function of undoped graphene and of related sp^2 carbon materials, graphite and nanotubes, always displays π and $\pi + \sigma$ plasmons, arising from interband transitions occurring below 10 eV and above 15 eV, respectively. We demonstrate that scattering geometry effects, encoded in the kinematic prefactor are responsible for a spectral reshaping akin to HREELS [23, 25, 38], need to be properly disentangled from the intrinsic dielectric response of the target in order to study the relative intensities of different EEL peaks and the low-dimensional effects on screening.

RESULTS AND DISCUSSION

2D kinematic factors

In the right panel of Fig. 1, we show the optical limit of the EEL cross section of graphite with a momentum resolution of $\Delta q = 0.1 \text{ \AA}^{-1}$ and of freestanding graphene at the higher momentum resolution ($\Delta q = 0.02 \text{ \AA}^{-1} \approx q_z$). We note the graphene cross section is completely quenched, as opposite to the case of graphite.

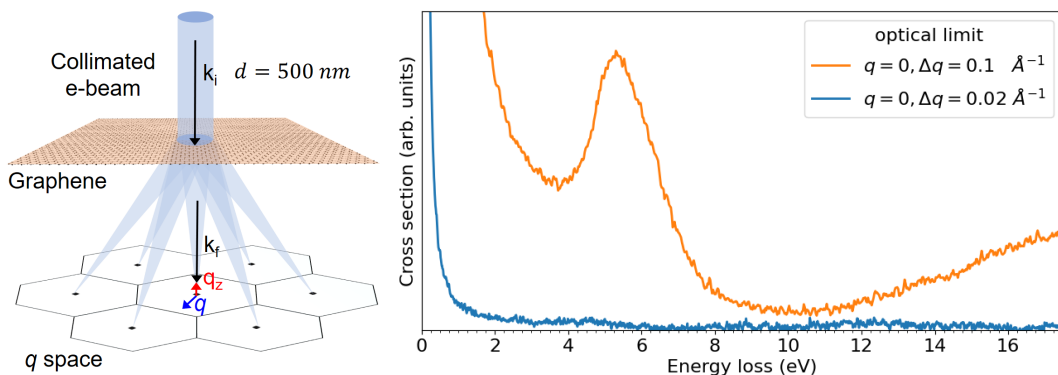


Figure 1: Left: parallel beam setup for momentum resolved EELS. The momentum transfer lost by the incoming electron along the direction parallel (perpendicular) to the beam, q_z (q), is shown in red (blue). Right: EEL cross section at vanishing momentum transfer of graphite with standard q resolution (orange) and of graphene with high resolution (blue).

As we derive in the supporting information, the electron energy-loss cross section of a 2D system near the optical limit may be written as

$$\frac{d^2 S}{d\Omega d\hbar\omega}(|\mathbf{q}| \approx 0, \omega) = \frac{4A^{u.c.}}{\pi^2 a_0^2} \frac{q^2}{(q^2 + q_z^2)^2} \frac{\text{Re}[\tilde{\sigma}(\omega)]}{\omega}, \quad (1)$$

where a_0 is the Bohr radius, $A^{\text{u.c.}}$ is the area of the 2D unit cell and $\tilde{\sigma}$ is the optical conductivity along the momentum transfer \mathbf{q} . The EEL cross section near the optical limit contains the same information as the optical coefficients (see supporting information for more details). However, the kinematic prefactor is $I_{kin} \equiv q^2/(q^2 + q_z^2)^2$, thus the cross section is quenched for $q \leq q_z$, even though the optical conductivity remains finite. Using energy and momentum conservation, q_z can be expressed as [1, 26]:

$$q_z(q, \omega) = k_i - \sqrt{k_i^2 - q^2 - 2m\omega/\hbar} \quad (2)$$

$$\approx \frac{m\omega}{\hbar k_i} + \frac{q^2}{2k_i} \quad (3)$$

where k_i and m are the wavenumber and mass of the incoming electron. The approximation in the second-line holds as the energy of the beam electrons, $E_i \gg \hbar\omega$ and $k_i \gg q$. The kinematic prefactor I_{kin} encompasses, through q_z , a non trivial dependence of the EELS cross section on both the energy loss $\hbar\omega$ and the electron beam energy E_i , as given in Eqs. (2)-(3). In order to ease its deconvolution from the intrinsic response in momentum-resolved spectra, it is convenient to introduce a spectral reshape function defined as

$$A(\mathbf{q}, \omega, E_i) \equiv \frac{q^4}{[q^2 + q_z^2(q, \omega, E_i)]^2}, \quad (4)$$

which connects the measured EELS cross section to the longitudinal dielectric response of the system. Since EEL spectra are always expressed up to a multiplicative constant that takes into account experimental parameters like exposure times, beam current etc., we define the spectral reshape function such that it equals one in the limit $q \rightarrow 0$ and $\omega \rightarrow 0$. Being $A(\mathbf{q}, \omega, E_i) = q^2 I_{kin}$, our definition can be safely applied to the analysis of momentum-resolved spectra at fixed q , and the intrinsic response of the target can be obtained as the EEL spectrum divided by the reshape function.

We show in Fig. 2 concrete examples of q_z and A dependencies on the energy loss $\hbar\omega$. In the top panel, we show q_z at $q = 0$ for different incoming electron energies E_i . We verified numerically that q_z is independent on q for the range considered ($q < 0.1 \text{ \AA}^{-1}$, $\hbar\omega \approx \text{eV}$). For 2D systems q_z should be considered as a critical q value under which the cross section is quenched due to 2D kinematic effects. In the lower panel of Fig. 2, we show A at several q . The incoming electron energy E_i is 30 keV. Each line shows the relative cross section drop due to the increase of q_z as a function on $\hbar\omega$. The drop in the signal is more pronounced at lower incoming energies E_i (not shown). At sufficiently small q , the signal is quenched in the $\hbar\omega$ range of the valence excitations. The grey areas in Fig. 2 correspond to the energy ranges of graphene plasmons. The signal reshaping is very strong in the π plasmon region at very low momentum transfer, while it becomes negligible at $q > 0.035 \text{ \AA}^{-1}$. Instead the reshaping in the energy range of the $\pi + \sigma$ plasmon is approximately linear in ω , and effective in the range of considered momentum transfer. q_z and A are system independent and thus apply to EEL spectra of any 2D system.

Spectral reshaping at low momentum transfers

In Fig. 3, we display with blue lines a set of EEL spectra measured at different low-momentum transfers q and a beam energy of 30 keV. We emphasize the reduced width of the ZLP attained with our experimental setup, where we adopt a pinhole-type aperture instead of a slit one. We show in the right panel of Fig. 3 a sketch of the direct beam and the pinhole-type aperture at the different \mathbf{q} . The two lowest pinhole positions correspond to the two spectra in the bottom of Fig. 3. They are clearly different from earlier reports [39–42], but also still affected by the direct beam. The unprecedented observation of kinematically quenched plasmon peaks is attributed to the q resolution of 0.02 \AA^{-1} . The pinhole-type aperture does not only block the direct beam well below 0.1 \AA^{-1} , it is also instrumental for observing the quenched plasmon peaks near the optical limit. In all the earlier reports [39–42] the loss spectra at the lowest q were always the ones with the strongest plasmon peaks, provided by the spurious inclusions of electrons with $q > q_z$, as $\Delta q > q_z$.

As the momentum transfer decreases down towards 0.030 \AA^{-1} , the $\pi + \sigma$ plasmon loses spectral weight with respect to the π plasmon. At even lower momentum transfers, $q < 0.030 \text{ \AA}^{-1}$, the spectral signatures of both the π and $\pi + \sigma$ plasmons become comparable or smaller than the noise level, i.e., they are below the detection limit. To highlight the effect, we also plot the $\times 40$ zooms of the spectra for the two lowest momenta in Fig. 3. At $q \approx 0.015 \text{ \AA}^{-1}$ a small trace of the π plasmon can still be discerned from the spectral noise but the $\pi + \sigma$ plasmon (not shown) is already indiscernible. As can be seen from the top panel of Fig. 2, $q \approx 0.015 \text{ \AA}^{-1}$ corresponds to the limit case where $q > q_z$

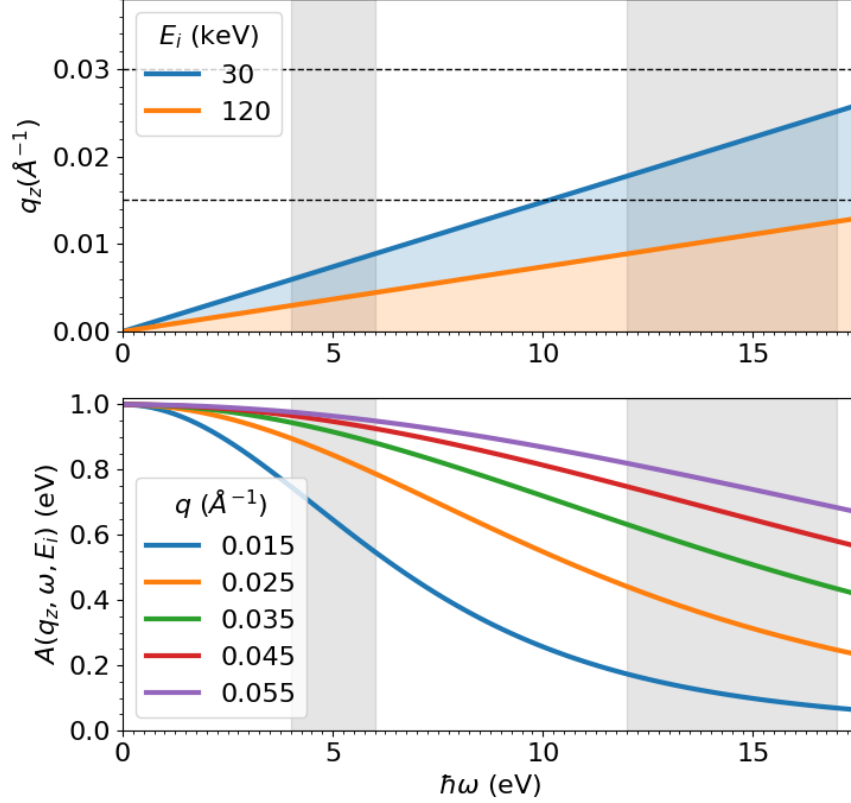


Figure 2: Energy loss dependence of q_z (top panel) and the reshape factor A (lower panel) for EEL spectra at different q and incident energies E_i . q_z is evaluated at $q = 0$, while A at $E_i = 30$ keV. Dashed horizontal lines in the top panel mark the lowest q values shown in Fig. 3. The π and $\pi + \sigma$ plasmons of graphene lie in the grey spectral regions.

in the π plasmon region and $q < q_z$ in the $\pi + \sigma$ plasmon region. At $q \approx 0.000 \text{ \AA}^{-1}$ the spectral noise is of the same order as the signal even in the energy range of the π plasmon. This is a clear signature of the cross section quenching due to kinematic effects at very low momentum transfer. The signal quenching can be appreciated if only electrons with $q \leq q_z$ are collected, thus for a q resolution with Δq at least on the order of q_z as in our experimental setup. Otherwise, spurious inclusions of electrons with $q > q_z$ would dominate the cross section signal. The faster quenching of the $\pi + \sigma$ spectral feature as opposed to the π plasmon is consistent with the expected effect captured by the reshape function A shown in Fig. 2. To further highlight the kinematic origin of the spectral reshaping in Fig. 3, we also plot with red lines the spectra divided by the reshape function A from Eq. (4). We excluded from this procedure the $q < 0.030 \text{ \AA}^{-1}$ spectra because of the too high noise enhancement. All such scaled spectra are normalized to have the same intensity as the originals at the π plasmon peak. The removal of kinematic effects increases the $\pi + \sigma$ intensity with respect to the π peak intensity. The decrease of the intensity ratio between the $\pi + \sigma$ and π peaks when approaching the optical limit is thus due to kinematic effects and it is not an intrinsic property of the dielectric response of graphene.

Intrinsic dielectric response of Graphene

In the top panel of Fig. 4, we show the ratio between the intensities of the π and $\pi + \sigma$ plasmons as a function of momentum transfer q for both the raw spectra and the dielectric response (obtained by dividing the spectra by A). Their spectral ratio $I_\pi/I_{\pi+\sigma}$ increases at lower momentum transfer due to the kinematic reshaping that lowers the intensity of the $\pi + \sigma$ plasmon more than that of the π plasmon. Once the signal is divided by the reshape function A

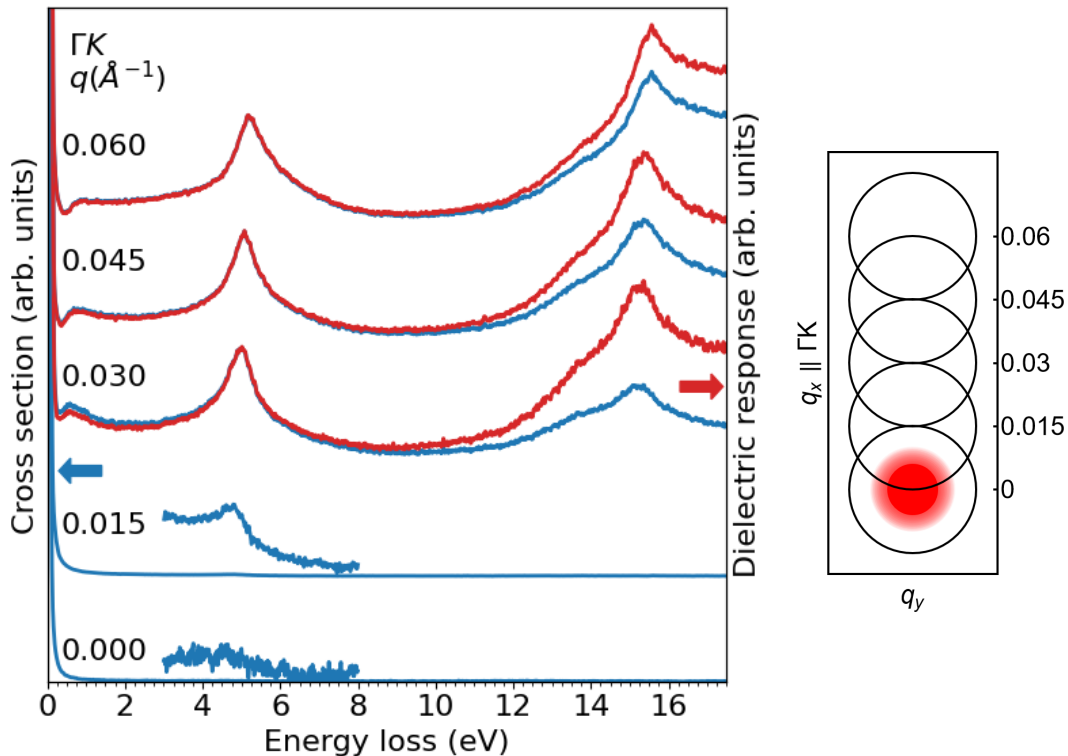


Figure 3: Left: low energy EELS spectra of freestanding graphene at finite q along the ΓK direction and the nominal $q = 0$ spectrum. We show also the $\times 40$ magnification of the two lower momentum transfer spectra in the range of the π plasmon ($[3, 8]$ eV). Red (blue) lines indicate EELS spectra (not) divided by the kinematic factor A . Right: sketch of the direct beam (red) and pin-hole aperture at different momentum transfers q .

and the intrinsic dielectric response is uncovered, the intensity ratio is instead approximately constant. According to Eq. (1), we deduce that in this regime the dielectric response is approximately converged to its optical value ($q = 0$), while kinematic effects are still very sensitive to small momentum transfer variations.

The finite accuracy of small momentum transfers is crucial for calculating A . We address the experimental accuracy in the lower panel of Fig. 4 by plotting the same intensity ratio with a momentum transfer \tilde{q} calibrated on the well established isotropic linear π plasmon dispersion [15, 43]. We note that a different momentum calibration does not just trivially change the \tilde{q} values in the spectral intensity ratios, but it also alters the intensity ratios, as A also changes. The qualitative picture is unchanged with the calibrated \tilde{q} , but the results are far less affected by experimental accuracy. The differences between q and \tilde{q} are below $\approx 0.02 \text{ \AA}^{-1}$, which is in line with the actual pixel size in the low magnification diffraction mode. \tilde{q} has the potential to become a valuable tools for further instrumental developments regarding small angle TEM-EELS. \tilde{q} can be determined from one single EEL spectrum of graphene and then the experimental q can be calibrated against \tilde{q} .

CONCLUSIONS

We studied the EEL cross section of graphene near the optical limit. We find the minimum observable q is limited by the condition $q \geq q_z$, where q_z is given by Eq. (3). At lower momentum transfers, we observed a quenching of the EELS cross section in freestanding graphene. We have revisited the role of kinematic and scattering geometry effects in TEM-EELS cross section of low-dimensional, freestanding materials. Our analysis shows that the kinematic prefactor, entailing the well known dependence on both the energy loss and the energy of the beam electrons, is responsible for a quenching of the EELS cross section of atomically thin specimen when approaching the optical limit, albeit the intrinsic 2D optical conductivity remains finite. High momentum resolution of TEM-EELS is instrumental to access the low-momentum transfer regime where such 2D kinematic effects emerge. In this respect, we argue that

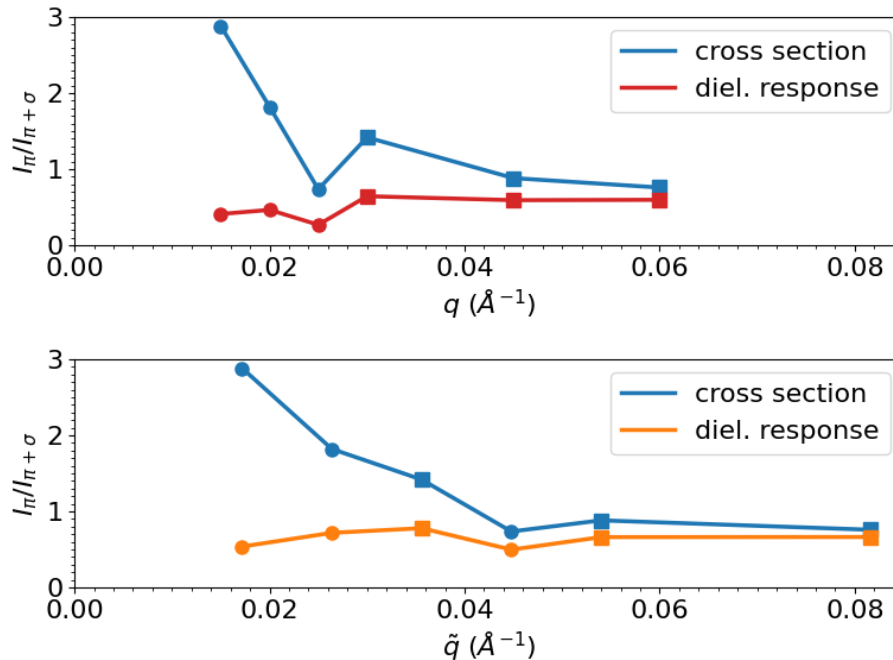


Figure 4: Ratio between the intensities of the π and $\pi + \sigma$ plasmons of graphene as a function of the momentum transfer q . The upper panel uses the experimental q . The lower panel uses \tilde{q} inferred from the isotropic π plasmon dispersion [15, 43]. Squares (circles) are q and \tilde{q} along the ΓM (TK) direction.

a wide collimated beam and a pinhole-type aperture in the diffraction plane are essential to achieve the best possible resolution required to go as close as possible to the optical limit. We emphasize however that our analysis is not limited to graphene, and it applies to any low-dimensional material of given thickness d whenever the conditions $q_z d \ll 1$ and $q d \ll 1$ are satisfied.

In order to ease the deconvolution of kinematic effects from the intrinsic 2D response of the target, we introduced a reshape function for momentum-resolved EEL spectra. When applied to EEL spectra of graphene, the reshape function indicates that the relative intensity reduction of the $\pi + \sigma$ plasmon with respect to the π plasmon is a pure kinematic effect, while the longitudinal dielectric response of the system approximately converges to its optical ($q \approx 0$) value.

Since the high magnification of the diffraction plane does not allow to measure simultaneously Bragg spots usually needed to calibrate the momentum transfer, we benchmarked our accuracy in q by comparing it against \tilde{q} that was calibrated with the isotropic π plasmon dispersion. The reshape function A from Eq. 4 is – via \tilde{q} – determined by the π plasmon position alone and can be directly checked against the relative strengths of the π and $\pi + \sigma$ plasmons in freestanding graphene. This may constitute an independent and self consistent way to calibrate and benchmark the next generation of high angular resolution TEM-EELS instruments.

Author Contributions

A.G., P.B. and F.M. developed the theoretical framework. Y.L. prepared the sample. R.S. and Y.L. performed the experiments. A.G. and C.K. analyzed the results. All authors contributed to discussion of the results. A.G., P.B., C.K., T.P. and F.M. wrote the manuscript.

Acknowledgements

R.S. and K.S. acknowledges the support for JST-CREST (JPMJCR20B1, JPMJCR20B5, JPMJCR1993). This project has received funding from the European Research Council (ERC) under the European Union’s Horizon 2020

research and innovation programe (MORE-TEM ERC-SYN project, grant agreement No 951215).

SUPPORTING INFORMATION

Experimental setup

Details on the sample preparation and specific conditions for EELS with an energy and momentum resolution (FWHM) of 45 meV and 0.02 \AA^{-1} , respectively, are given in Ref. [15]. A sketch of our experimental setup is displayed in the left panel of the letter Fig. 1. The JEOL3C2 TEM was operated at 30 kV, with a beam current of about 10 pA. The individual spectra are sums of 300 to 500 individual acquisitions with dwell times ranging between 1 ms and 1 s.

The resolution in q depends on the electron wavenumber k_i , the half convergence angle (α) of the incoming beam as well as the half collection angle (β) defined by the aperture in the diffraction plane and the camera length. With the 500 nm wide beam we achieve $q_\alpha = k_i \sin \alpha = 0.006 \text{ \AA}^{-1}$ and $q_\beta = k_i \sin \beta = 0.015 \text{ \AA}^{-1}$. The beam path stability amounts to an additional shared uncertainty of $q_\vartheta = k_i \sin \vartheta = 0.004 \text{ \AA}^{-1}$. The resolution is thus given by

$$\Delta q = k_i \left(\sqrt{\sin^2 \alpha + \sin^2 \beta} + \sin \vartheta \right) = 0.02 \text{ \AA}^{-1} . \quad (5)$$

In the left panel of Fig. 5 we plot the spatial and momentum resolution used in this work with the JEOL3C2 setup, alongside those obtained using other TEM setups [9–15]. The spot size determines the spatial resolution as well as the diffraction (Abbe) limit of the convergence angle α , that could be attained only with perfect aberration correction. As shown in the left panel of Fig. 5, the achieved beam parameters q_α and q_β are well above the Abbe limit of diffraction. For optimal performance the collection angle β must be big enough for α and ϑ . Smaller β lose intensity without any meaningful effect in Δq . We did not include very asymmetric settings $\beta \ll \alpha$ with longer camera lengths (e.g. Ref. [44]), as q_β alone is not comparable to Δq . In the central panel of Fig. 5, we show a TEM image of the sample, along with a red mark with 500 nm diameter. This is the size of the collimated beam for the diffraction image in the right panel and the EELS measurements.

The zero-loss peak (ZLP) becomes more and more intense as the aperture approaches the optical limit. This challenges the possibility to observe the predicted quenching of the loss function. In order to lessen the impact of the ZLP, the profile of the direct beam in the diffraction plane must not hit the aperture. This should arguably always be easier to achieve with a pinhole-type aperture than with a slit.

The challenge with the very high momentum resolution and the according highly magnified diffraction planes is that the Bragg spots can not be recorded simultaneously, hence they cannot be used to establish the magnitude of q . The accuracy of the position in the diffraction plane is intrinsically limited to the pixel size (0.02 \AA^{-1}) in the overview diffraction pattern in the right panel of Fig. 5. The stability of the beam and reproducibility of the electron optics can be verified by checking for shifts when repeatedly zooming in and out.

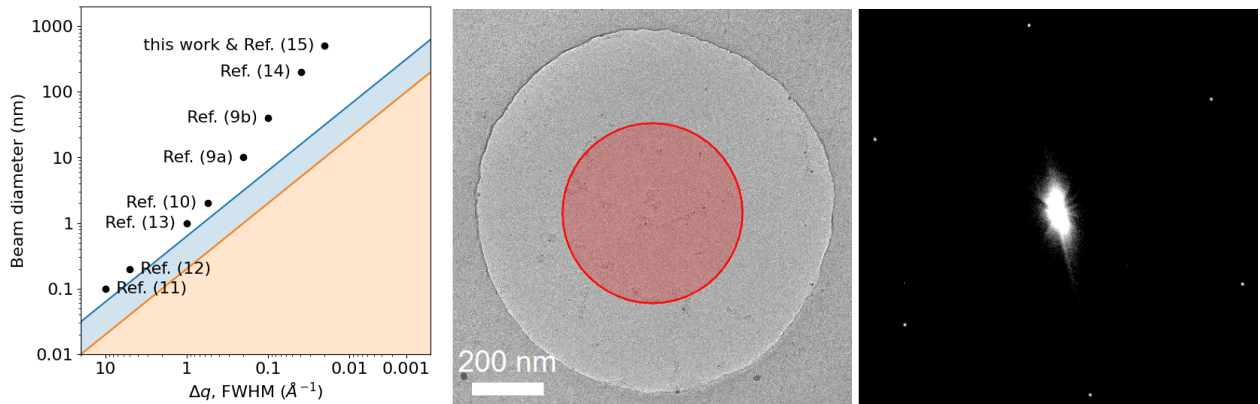


Figure 5: Left: achieved resolutions in q above the blue Abbe diffraction and orange Heisenberg uncertainty limits. Center: overview TEM micrograph. The size of the collimated beam is marked in red. Right: low magnification (x0.2) diffraction pattern.

EELS cross section of a 2D material at small momentum transfer

We consider a high energy electron incoming to a 2D material with momentum k_i perpendicular to the layer and energy $E_i = \hbar^2 k_i^2 / 2m$, where m is the electron mass. Within scattering theory in the Born approximation [7, 31], the (transmission) EELS differential cross section is given by

$$\frac{d^2 S}{d\Omega d\hbar\omega}(\mathbf{q}, \omega) = \frac{4A^{u.c.}}{\pi^2 a_0^2} \frac{1}{(q^2 + q_z^2)^2} \text{Im} \left[- \iint dz dz' e^{iq_z(z-z')} \chi(\mathbf{q}, z, z', \omega) \right], \quad (6)$$

where a_0 is the Bohr radius, and $A^{u.c.}$ is the area of the 2D unit cell. The density-density response function of the system, defined as $\chi \equiv \delta\rho^{(1)}/\delta\phi^{ext}$, with ϕ^{ext} the perturbing scalar potential and $\rho^{(1)}$ the induced charge density, is Fourier transformed along the 2D periodic direction of the system in terms of the in-plane component of the momentum transfer \mathbf{q} . The out-of-plane momentum transfer q_z cannot be interpreted in terms of crystalline quasi-momentum of the 2D system, that is defined only along the periodic directions, being instead formally accounted for by the double-integral along z and the complex exponential in Eq. (6). In other words, q_z is a good quantum number for the incident electron but not for the electrons of the system, while q is a good quantum number for both kinds of electrons. If the system is composed by a sufficiently high amount of layers, the integrals in Eq. (6) give approximately the Fourier transforms along z and z' , and one recovers the bulk approximation for thick films.

Since we are interested in valence band excitations ($\hbar\omega \approx 1-20$ eV), with standard experimental setups ($E_i \approx 30$ keV, $k_i \approx 88.73 \text{ \AA}^{-1}$), q_z ranges between 10^{-3} and 10^{-2} \AA^{-1} when approaching the optical limit $\mathbf{q} \rightarrow 0$. It follows that for atomically thin samples ($d \approx 1-5 \text{ \AA}$) and in the low-momentum transfer regime, the complex exponential in Eq. (6) may be approximated to unity and the intrinsic dielectric response of the systems becomes independent of q_z . On the other hand, the presence of a finite q_z in the denominator in front of the density-density response of Eq. (6) removes the diverging behaviour of the cross section when approaching the optical limit.

We are interested in the limit of small momentum transfers. If $qd \ll 1$, finite thickness effects are negligible and the system may be modeled with a dielectric sheet located at $z = 0$ [32]. In this limit, it is possible to define a 2D inverse dielectric function [32]

$$\varepsilon_{2D}^{-1}(\mathbf{q}, \omega) \equiv 1 + v_{2D}(q) \tilde{\chi}(\mathbf{q}, \omega), \quad (7)$$

where $v_{2D} = e^2/2\varepsilon_0 q$ is the 2D Fourier transform of the Coulomb potential and $\tilde{\chi}(\mathbf{q}, \omega) \equiv \iint dz dz' \chi(\mathbf{q}, z, z', \omega)$. The EELS differential cross section of Eq. (6) may thus be written in terms of the 2D inverse dielectric function as

$$\frac{d^2 S}{d\Omega d\hbar\omega}(\mathbf{q}, \omega) = \frac{8\varepsilon_0 A^{u.c.}}{\pi^2 e^2 a_0^2} \frac{q}{(q^2 + q_z^2)^2} \text{Im} [-\varepsilon_{2D}^{-1}(\mathbf{q}, \omega)] , \quad (8)$$

thus taking the form of a product between a purely kinematic factor $q/(q^2 + q_z^2)^2$ and the 2D loss function, in close analogy with the expression of HREELS cross section [21, 22, 24]. In addition, the long-wavelength limit of the 2D dielectric function may be written as [33]

$$\varepsilon_{2D}(\mathbf{q} \rightarrow 0, \omega) \approx 1 + i \frac{\tilde{\sigma}(\omega) e^2 q}{2\varepsilon_0 \omega}, \quad (9)$$

where $\tilde{\sigma}(\omega) \equiv \hat{\mathbf{q}} \cdot \boldsymbol{\sigma}_{2D}(\omega) \cdot \hat{\mathbf{q}}$, and $\sigma_{2D}^{ij} = \delta j_{2D}^{(1),i} / \delta E^j$ is the 2D optical conductivity, relating the total electric field with the induced current density at $z = 0$. Except for the case of acoustic plasmons, in the limit of small momentum transfers $\varepsilon_{2D}(\mathbf{q} \rightarrow 0, \omega)$ linearly approaches unity (see Eq. 9), as shown in the static case for 2D semiconductors [45–47], and the imaginary part of ε_{2D} vanishes. From a physical perspective, the above limit may be understood as follows: in the case of two far apart test charges (i.e. in the long-wavelength limit), the 2D system is not able to screen the Coulomb interaction, as the vast majority of field lines bypass the material. The conductivity is instead finite, as finite current densities are allowed in the long-wavelength limit: the conductivity of graphene at zero momentum transfer is indeed the quantized conductance [48].

By inserting Eq. (9) into Eq. (8) the EELS cross section may be written as

$$\frac{d^2 S}{d\Omega d\hbar\omega}(|\mathbf{q}| \approx 0, \omega) = \frac{4A^{u.c.}}{\pi^2 a_0^2} \frac{q^2}{(q^2 + q_z^2)^2} \frac{\text{Re} [\tilde{\sigma}(\omega)]}{\omega}. \quad (10)$$

Because of the overall kinematic prefactor $I_{kin} \equiv q^2/(q^2 + q_z^2)^2$, the cross section is quenched when the in-plane component q of the momentum transfer q_{3D} approaches zero, even though the optical conductivity remains finite.

There is no possibility for the incoming electrons to excite a 2D system without also transferring a finite in-plane momentum q , as the intrinsic response of the system depends only on the latter. This feature is unique to low-dimensional systems, and is not captured by the bulk 3D approximation of the TEM-EELS cross section, that should apply only to thick enough films.

According to Eq. (1), the cross section quenching should be detected when $q \leq q_z$. As q_z is of the order of 0.01 \AA^{-1} in standard experimental setups, the momentum resolution should be at most of the same order of magnitude to reach the low-momentum transfer regime in experiments. On the other hand, $d \approx 3.5 \text{ \AA}$ in freestanding graphene, implying that at $q \leq 0.1 \text{ \AA}^{-1}$ both conditions $q_z d \ll 1$ and $qd \ll 1$ are satisfied.

Optical properties and electron energy loss

The vanishing momentum transfer regime is also referred to as the optical limit, since photons transfer negligible momentum to the electrons. In the literature, it is generally accepted that in the long-wavelength limit ($q \rightarrow 0$) the EELS cross section provides the same information as optical absorption for 2D systems, as (finite-energy) collective excitations are quenched [49]. The reflection and transmission coefficients of a 2D sheet for light polarized along one of its principal axes are

$$\mathcal{R}(\omega) = \left| \frac{Z_0 \tilde{\sigma}(\omega)}{2 + Z_0 \tilde{\sigma}(\omega)} \right|^2, \quad (11)$$

$$\mathcal{T}(\omega) = \left| \frac{2}{2 + Z_0 \tilde{\sigma}(\omega)} \right|^2, \quad (12)$$

where $\tilde{\sigma}(\omega)$ is the optical ($q = 0$) conductivity along the principal axis, and $Z_0 = \sqrt{\mu_0/\epsilon_0} \approx 377 \text{ \Omega}$ is the vacuum impedance. The optical absorption coefficient $\mathcal{A}(\omega)$ may be obtained from the total energy conservation: $\mathcal{A} + \mathcal{R} + \mathcal{T} = 1 \forall \omega$. Both optical absorption and EELS probe the same response function, the optical conductivity. Thus, the two experiments are linked by Eqs. (1) and (11)-(12). In addition, up to first order in $\tilde{\sigma}$, i.e., not in the resonant excitation regime, $\mathcal{R}(\omega) \approx 0$ and $\mathcal{A}(\omega) \approx 1 - \mathcal{T}(\omega) \propto \text{Re}[\tilde{\sigma}]$, as the EEL cross section.

In principle, therefore, optical conductivity information is embedded both in the absorption coefficient and in EEL spectra at low momentum transfer. However, the EELS cross section of Eq. (1) also depends on the kinematic prefactor I_{kin} , that is quenched in the very same regime of small momentum transfer. To access the intrinsic optical conductivity of the system, therefore, one has to appropriately account for kinematic effects in the low- q EEL spectra.

* Electronic address: alberto.guandalini@uniroma1.it

- [1] R. F. Egerton, *Electron Energy-Loss Spectroscopy in the Electron Microscope* (Springer, 2011).
- [2] H. Ibach and D. Mills, *Electron Energy Loss Spectroscopy and Surface Vibrations* (Academic Press, 1982).
- [3] G. Mondio, F. Neri, S. Patanè, A. Arena, G. Marletta, and F. Iacona, *Thin Solid Films* **207**, 313 (1992), ISSN 0040-6090, URL <https://www.sciencedirect.com/science/article/pii/004060909290143Y>.
- [4] J. Hong, M. Koshino, R. Senga, T. Pichler, H. Xu, and K. Suenaga, *ACS Nano* **15**, 7783 (2021), pMID: 33818068, URL <https://doi.org/10.1021/acsnano.1c01868>.
- [5] X. Zhu, Y. Cao, S. Zhang, X. Jia, Q. Guo, F. Yang, L. Zhu, J. Zhang, E. W. Plummer, and J. Guo, *Review of Scientific Instruments* **86**, 083902 (2015), ISSN 0034-6748.
- [6] R. F. Egerton, *Reports on Progress in Physics* **72**, 016502 (2008).
- [7] K. Sturm, *Zeitschrift für Naturforschung A* **48**, 233 (1993).
- [8] V. Keast, *Calculating EELS Transmission Electron Microscopy: Diffraction, Imaging and Spectroscopy* (Springer, 2016).
- [9] R. Senga, K. Suenaga, P. Barone, S. Morishita, F. Mauri, and T. Pichler, *Nature* **573**, 247 (2019).
- [10] N. Li, X. Guo, X. Yang, R. Qi, T. Qiao, Y. Li, R. Shi, Y. Li, K. Liu, Z. Xu, et al., *Nature Materials* **20**, 43 (2020).
- [11] F. S. Hage, G. Radtke, D. M. Kepaptsoglou, M. Lazzeri, and Q. M. Ramasse, *Science* **367**, 1124 (2020).
- [12] R. Senga, Y.-C. Lin, S. Morishita, R. Kato, T. Yamada, M. Hasegawa, and K. Suenaga, *Nature* **603**, 68 (2022).
- [13] F. S. Hage, R. J. Nicholls, J. R. Yates, D. G. McCulloch, T. C. Lovejoy, N. Dellby, O. L. Krivanek, K. Refson, and Q. M. Ramasse, *Science Advances* **4**, eaar7495 (2018), <https://www.science.org/doi/pdf/10.1126/sciadv.aar7495>.
- [14] J. Hong, R. Senga, T. Pichler, and K. Suenaga, *Phys. Rev. Lett.* **124**, 087401 (2020).
- [15] A. Guandalini, R. Senga, Y.-C. Lin, K. Suenaga, A. Ferretti, D. Varsano, A. Recchia, P. Barone, F. Mauri, T. Pichler, et al., *Nano Letters* **23**, 11835 (2023).

- [16] T. Pichler, M. Knupfer, M. S. Golden, J. Fink, A. Rinzler, and R. E. Smalley, *Physical Review Letters* **80**, 4729 (1998).
- [17] R. Neudert, M. Knupfer, M. S. Golden, J. Fink, W. Stephan, K. Penc, N. Motoyama, H. Eisaki, and S. Uchida, *Phys. Rev. Lett.* **81**, 657 (1998).
- [18] R. Schuster, M. Knupfer, and H. Berger, *Phys. Rev. Lett.* **98**, 037402 (2007).
- [19] C. Kramberger, R. Hambach, C. Giorgetti, M. H. Rummeli, M. Knupfer, J. Fink, B. Buchner, L. Reining, E. Einarsson, S. Maruyama, et al., *Physical Review Letters* **100**, 196803 (2008).
- [20] R. Schuster, R. Kraus, M. Knupfer, H. Berger, and B. Büchner, *Phys. Rev. B* **79**, 045134 (2009).
- [21] D. Mills, *Surface Science* **48**, 59 (1975), ISSN 0039-6028.
- [22] P. Lambin, J. P. Vigneron, A. A. Lucas, and A. Dereux, *Physica Scripta* **35**, 343 (1987).
- [23] R. E. Palmer, J. F. Annett, and R. F. Willis, *Phys. Rev. Lett.* **58**, 2490 (1987).
- [24] C. Hogan, M. Palummo, and R. Del Sole, *Comptes Rendus Physique* **10**, 560 (2009).
- [25] J. Li, Z. Lin, G. Miao, W. Zhong, S. Xue, Y. Li, Z. Tao, W. Wang, J. Guo, and X. Zhu, *Surface Science* **721**, 122067 (2022), ISSN 0039-6028.
- [26] F. Roth, A. König, J. Fink, B. Büchner, and M. Knupfer, *Journal of Electron Spectroscopy and Related Phenomena* **195**, 85 (2014), ISSN 0368-2048.
- [27] A. C. Ferrari, F. Bonaccorso, V. Fal'ko, K. S. Novoselov, S. Roche, P. Bøggild, S. Borini, F. H. L. Koppens, V. Palermo, N. Pugno, et al., *Nanoscale* **7**, 4598 (2015), URL <http://dx.doi.org/10.1039/C4NR01600A>.
- [28] G. R. Bhimanapati *et al.*, *ACS Nano* **9**, 11509 (2015).
- [29] S. Y. Woo, A. Zobelli, R. Schneider, A. Arora, J. A. Preuß, B. J. Carey, S. Michaelis de Vasconcellos, M. Palummo, R. Bratschitsch, and L. H. G. Tizei, *Phys. Rev. B* **107**, 155429 (2023).
- [30] R. J. Nicholls, *Journal of Physics: Materials* **4**, 024008 (2021).
- [31] V. U. Nazarov, *New Journal of Physics* **17**, 073018 (2015).
- [32] T. Sohler, M. Calandra, and F. Mauri, *Phys. Rev. B* **91**, 165428 (2015).
- [33] P. Cudazzo, I. V. Tokatly, and A. Rubio, *Phys. Rev. B* **84**, 085406 (2011).
- [34] A. H. Castro Neto, F. Guinea, N. M. R. Peres, K. S. Novoselov, and A. K. Geim, *Rev. Mod. Phys.* **81**, 109 (2009).
- [35] F. Bonaccorso, Z. Sun, T. Hasan, and A. C. Ferrari, *Nature Photonics* **4**, 611 (2010).
- [36] A. Grigorenko, M. Polini, and K. Novoselov, *Nature Photon.* **6**, 749 (2012).
- [37] F. J. García de Abajo, *ACS Photonics* **1**, 135 (2014).
- [38] R. Palmer, J. Annett, and R. Willis, *Surface Science* **189-190**, 1009 (1987), ISSN 0039-6028.
- [39] M. K. Kinyanjui, C. Kramberger, T. Pichler, J. C. Meyer, P. Wachsmuth, G. Benner, and U. Kaiser, *Epl* **97**, 57005 (2012).
- [40] P. Wachsmuth, R. Hambach, M. K. Kinyanjui, M. Guzzo, G. Benner, and U. Kaiser, *Physical Review B* **88**, 075433 (2013).
- [41] F. J. Nelson, J.-C. Idrobo, J. D. Fite, Z. L. Mišković, S. J. Pennycook, S. T. Pantelides, J. U. Lee, and A. C. Diebold, *Nano Letters* **14**, 3827 (2014).
- [42] S. C. Liou, C.-S. Shie, C. H. Chen, R. Breitwieser, W. W. Pai, G. Y. Guo, and M.-W. Chu, *Physical Review B* **91**, 045418 (2015).
- [43] P. Wachsmuth, R. Hambach, G. Benner, and U. Kaiser, *Physical Review B* **90**, 235434 (2014).
- [44] P. Midgley, *Ultramicroscopy* **76**, 91 (1999).
- [45] D. Y. Qiu, H. Felipe, and S. G. Louie, *Phys. Rev. B* **93**, 235435 (2016).
- [46] F. Hüser, T. Olsen, and K. S. Thygesen, *Phys. Rev. B* **88**, 245309 (2013).
- [47] A. Guandalini, P. D'Amico, A. Ferretti, and D. Varsano, *npj Computational Materials* **9**, 44 (2023).
- [48] N. Tombros, A. Veligura, J. Junesch, M. Guimarães, I. J. Vera-Marun, H. T. Jonkman, and B. J. van Wees, *Nature Physics* **7**, 697 (2011).
- [49] F. Stern, *Physical Review Letters* **18**, 546 (1967).